Fe-O-Fe-bridged porphyrin network membranes for solvent-resistant nanofiltration

Wang, Zheng ; Nakagawa, Keizo ; Guan, Kecheng ; Zhang, Aiwen ; Okamoto, Yasunao ; Matsuoka, Atsushi ; Kamio, Eiji ; Yoshioka, Tomohisa ;…

(Citation)
Journal of Membrane Science,737:124485

(Issue Date)
2026-01

(Resource Type)
journal article

(Version)
Version of Record

Journal of Membrane Science 737 (2026) 124485

Contents lists available at ScienceDirect

Journal of Membrane Science

journal homepage: www.elsevier.com/locate/memsci

Fe–O–Fe-bridged porphyrin network membranes for solvent-resistant nanofiltration

Zheng Wang [a], Keizo Nakagawa [b,c,*], Kecheng Guan [c], Aiwen Zhang [a], Yasunao Okamoto [c], Atsushi Matsuoka [a,c], Eiji Kamio [a,c], Tomohisa Yoshioka [b,c], Hideto Matsuyama [a,c,**]

[a] Department of Chemical Science and Engineering, Kobe University, 1-1 Rokkodai, Nada, Kobe, 657-8501, Japan
[b] Graduate School of Science, Technology and Innovation, Kobe University, 1-1 Rokkodai, Nada, Kobe, 657-8501, Japan
[c] Research Center for Membrane and Film Technology, Kobe University, 1-1 Rokkodai, Nada, Kobe, 657-8501, Japan

ARTICLE INFO

Keywords:
Porphyrin network
Metal coordination
Solvent-resistant nanofiltration
Polar aprotic solvent
Anti-swelling

ABSTRACT

The stability of solvent-resistant nanofiltration (SRNF) membranes, such as integrally skinned asymmetric (ISA) and thin-film composite (TFC) membranes, in polar aprotic solvents must be improved if they are to meet increasingly complex industrial demands. The stability of the former membranes can be improved by forming crosslinked rigid chains, such as polybenzimidazoles and polyimides, but this requires time-consuming treatment processes. Conversely, the latter membranes are easy to fabricate but lack efficient active sites for crosslinking and structural rigidity. Herein, we present a fabrication strategy combining the characteristics of both types of membranes. We first utilize amino-functional porphyrins as polyaromatic units to form rigid polyamide networks by vacuum-assisted interfacial polymerization, simultaneously providing active sites for further crosslinking, which is accomplished by immersion in $FeCl_2$/dimethyl sulfoxide (DMSO) solution to directly establish Fe–*O*–Fe bridges between porphyrin centers to form a stable network. The Fe–*O*–Fe-bridged porphyrin networks are solvent-stable in DMSO. Furthermore, they achieve outstanding molecular separation (96.2 % rejection of methyl orange, 327 Da) and limited molecular-weight-cutoff change (from 360 to 420 Da) during alternating MeOH and DMSO filtration, along with long-term recovery efficiency (>96.7 % over seven days). Thus, our study provides a promising strategy for the facile development and fabrication of efficient, robust SRNF membranes.

1. Introduction

Solvent-resistant nanofiltration (SRNF) is a green and low-cost alternative to industrial separation techniques such as distillation, adsorption, and extraction. However, its industrial application remains challenging and immature compared to membranes used for aqueous environments [1–3]. Because the electrostatic interaction between membranes and molecules is generally limited in organic solvents than in water, the separation efficiency of SRNF typically relies on size-sieving to realize solvent-solute separation in the range 200–1000 Da, which demands precise control of pore size and distribution [4].

Polar aprotic solvents exhibit excellent solubilization properties owing to their midrange lipophilicities, allowing recovery of both the acidic and basic moieties involved in SN_2-type reactions common in pharmaceutical synthesis. Dimethyl sulfoxide (DMSO) is a non-toxic and green solvent manufactured from lignin and dimethyl sulfide. DMSO can replace NMP, DMF, and DMAc, but it has a high boiling point and low vapor pressure, making membrane separation more suitable than a heat-driven recovery [5–7]. DMSO is also widely used in membrane fabrication because of its high affinity to polymer fragments and aromatic building blocks, according to Hansen solubility parameters [8,9]. This implies that the separation efficiency of a membrane in DMSO will deteriorate as a result of partial redissolving or the swelling of membrane networks [10,11]. Therefore, the development of strategies to form SRNF membranes featuring robust and regular networks is necessary.

Over the past decade, crosslinked polyimide and polybenzimidazole membranes have emerged for SRNF because their rigid fragments impart chemical and mechanical tolerances. The membrane fabrication process involves a consistent sequence that includes nonsolvent-induced phase separation (NIPS) and post-treatment [12]. NIPS utilizes the high solubility of the polymer and additives in polar aprotic solvents for

* Corresponding author. Graduate School of Science, Technology and Innovation, Kobe University, 1-1 Rokkodai, Nada, Kobe, 657-8501, Japan.
** Corresponding author. Department of Chemical Science and Engineering, Kobe University, 1-1 Rokkodai, Nada, Kobe, 657-8501, Japan.
E-mail addresses: k.nakagawa@port.kobe-u.ac.jp (K. Nakagawa), matuyama@kobe-u.ac.jp (H. Matsuyama).

https://doi.org/10.1016/j.memsci.2025.124485
Received 13 May 2025; Received in revised form 26 June 2025; Accepted 25 July 2025
Available online 29 July 2025

simple membrane fabrication, while post-treatment exposes membranes to a crosslinker and initiator to form three-dimensional or interpenetrating networks to enhance their stability in polar aprotic solvents [5,13–15]. To avoid pathway block of those short chains, organic acids, CuI and metal ions were also introduced to form electrostatic interaction or coordination bonds [16,17]. For example, Jin et al. reported crosslinked polyimide membranes based on a carboxyl-functionalized polyimide backbone bearing diamino-benzoic acid Cu^{2+} coordination sites [18]. They exhibit good stability in a variety of organic solvents, including DMF, and achieve 96 % rejection of Coomassie Brilliant Blue (854 Da). Such modifications have proven efficient for SRNF membranes. However, they are limited in terms of suitable polymers, and their preparation involves time-consuming procedures and biotoxic compounds.

Polyamide (PA) membrane fabrication via interfacial polymerization (IP) offers an attractive alternative approach because of tunable molecular networks, which are formed between amine monomers and acyl chlorides. However, polar aprotic solvents have a higher affinity with it, thereby dissolving any low molecular weight oligomers generated during polymerization and swelling the formed dense part [19]. Accordingly, as the polarity of the solvent increases (NMP < DMF < DMSO), the change in molecular weight cutoff (MWCO) for the membrane increases [20,21]. Several studies have shown that PA membranes prepared using *m*-phenylenediamine (MPD) and trimesoyl chloride (TMC) exhibit stable membrane performance in DMSO, but their rejection performances were assessed using solute molecules much larger than the MWCO of the studied membrane [22]. Similar to crosslinked polyimide and polybenzimidazole membranes, rigid networks can be obtained using polyaromatic monomers, such as tetra-(4-aminophenyl) ethylene, and covalent organic framework (COF) monomers [23,24]. Expectantly, those crosslinks could be further applied to enhance the solvent stability of PA networks in polar aprotic solvents. Recently, Feng et al. reported a reticularly crosslinked PA with a higher solvent resistance than that of linear or branched structures, which was attributed to the highly crosslinked network limiting polymer mobility, and its decreased surface area reduced membrane solubility [19].

In the present study, to improve the structural rigidity and introduce additional crosslinks, we developed porphyrin-based networks bridged by Fe–*O*–Fe bonds to form SRNF membranes. As Fig. 1a shows, the porphyrin unit was used as the polyaromatic block to supply primary solvent resistance, and its center is regarded as a coordination site for metal ions. Following our previous work, the IP reaction between 5,10,15,20-tetrakis(4-aminophenyl)-21H,23H-porphyrin (TAPP) and isophthaloyl chloride (IPC) was used to form a two-dimensional covalent organic network with the low MWCO of ~300 Da imparted by offset stacking [25]. Then, a novel metal-bridge crosslinking method inspired by *heme*-catalyzed oxygen reduction was easily performed by immersing the porphyrin membrane in a DMSO solution of $FeCl_2$ [26–28]. The bridged membrane exhibited minimal swelling and oligomer leakage, with stable network formation and long-term separation efficiency based on experiments using the model solute (*Z*)-2-(2-amino-4--thiazolyl)-2-methoxycarbonylmethoxyiminoacetic acid (NICA), an important side chain intermediate in the synthesis of the 3rd and 4th generation cephalosporins, in repeated MeOH and DMSO solvent filtration cycles (Fig. 1b).

2. Experimental section

2.1. Materials

All reagents were obtained from commercial suppliers and used without further purification. The organic-solvent-resistant polyketone substrate was prepared using a 14 wt% casting solution, as described in our previous works [29]. Anodic aluminum oxide (AAO; Whatman, Wilmington, Delaware, USA) was used as the porous substrate for characterization. 5,10,15,20-tetrakis(4-aminophenyl)-21H,23H-porphyrin (TAPP; 674.79 mg $mmol^{-1}$, 98 %, TCI, Tokyo, Japan), MPD (108.14 mg $mmol^{-1}$ Sigma-Aldrich, St. Louis, MO, USA), IPC (203.02

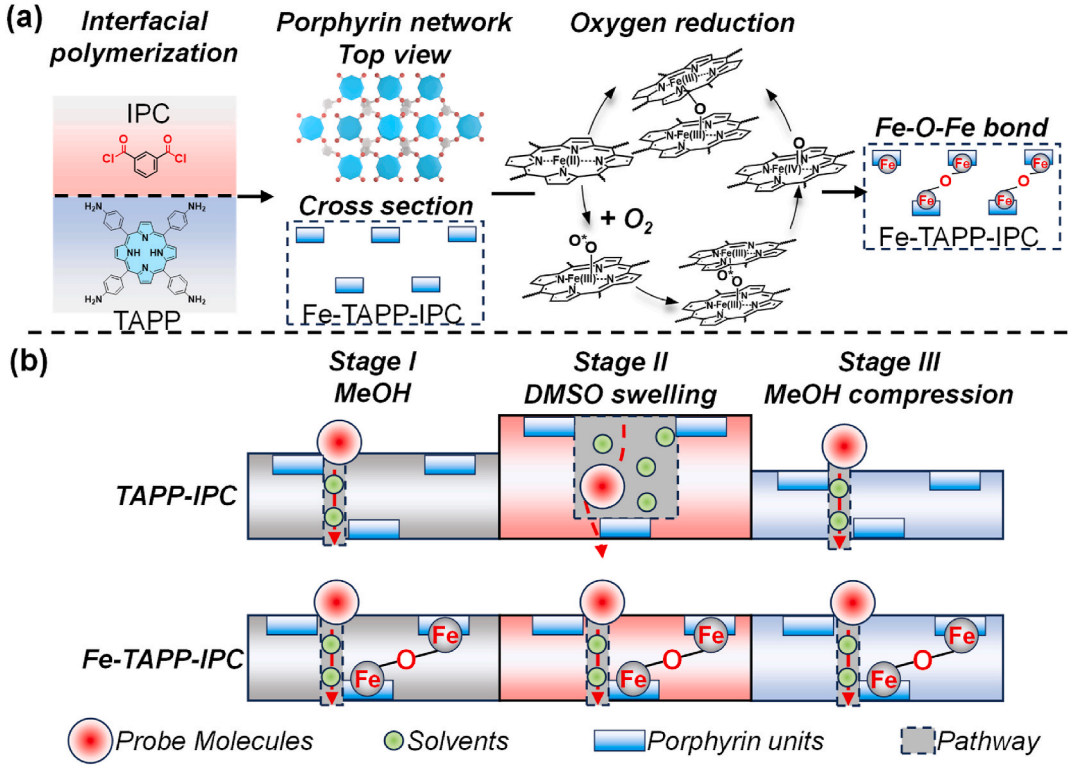

Fig. 1. a) Illustration of the membrane fabrication process and post-treatment for the introduction of Fe–*O*–Fe bridges. b) Possible swelling behaviors of different porphyrin membranes during MeOH-DMSO operation cycles.

mg $mmol^{-1}$, 99.0 %, TCI), and TMC (265.48 mg $mmol^{-1}$, Sigma-Aldrich) were used as the membrane monomers. HCl (0.05 M), metal ion sources ($FeCl_2$, $CuCl_2$, $ZnCl_2$, $AlCl_3$, and $FeCl_3$), and solvents (MeOH, EtOH, 1-propanol, and 1-butanol) were purchased from FUJIFILM Wako Pure Chemical (Osaka, Japan). Probe molecules of various molecular weights were used to evaluate the rejection performance. They included Methyl Orange (MO; 327 Da, FUJIFILM Wako Pure Chemical), NICA (Aladdin, Shanghai, China), and a series of polypropylene glycol (PPG), including 400, 725, and 1000 Da (Sigma-Aldrich).

2.2. Membrane fabrication

TAPP-based PA network membranes were fabricated using a previously reported method with slight modification [25]. Briefly, TAPP (1.2 mg mL^{-1}, ~0.0018 mmol mL^{-1} in 0.0375 M HCl aqueous solution and IPC (0.09 wt%, 0.565 mmol g^{-1})/TMC (0.15 wt%) in hexane solution were poured sequentially into a membrane fabrication device consisting of a PTFE frame (8 × 8 × 0.5 cm, inner diameter 6 cm), a fixed polyketone substrate, and a vacuum filtration system. After a 14-min reaction, the aqueous solution was removed by vacuum filtration (~1 min). The hexane solution was replaced with fresh *n*-hexane and MeOH several times. For comparison, a conventional PA membrane was prepared by traditional IP between MPD (2 wt%) and TMC (0.15 wt%) with a 2 min reaction time [30]. The above membranes are labeled TAPP-IPC and MPD-TMC according to the monomers.

2.3. Post-treatment with metal ions

According to the previous modification of porphyrin [31], the fresh membranes were washed with a MeOH/DMSO (1:1) mixture under vacuum filtration for 20 min. At the optimized condition, those membranes were immersed in 20 mL 16.25 mg mL^{-1} (0.128 mmol mL^{-1}) $FeCl_2$ DMSO solution and reacted in a 65 °C oven for 20 h. Here, DMSO works to swell PA network and to remove unreacted monomers and the low molecular weight oligomers. Finally, they were washed and reserved in MeOH before the following tests, the final membranes were named Fe-TAPP-IPC and Fe-MPD-TMC.

2.4. Membrane characterization

Field-emission scanning electron microscopy with an Os coating device (FE-SEM; JSM-IT800, JEOL Ltd., Tokyo, Japan) and atomic force microscopy (AFM; SPA 400, Hitachi Ltd., Tokyo, Japan) were used to explore the surface morphologies, cross-sectional thickness changes (i.e., swelling), and Energy dispersive spectroscopy (EDS) of the membranes. The chemical structures and elemental compositions of various samples were evaluated using Fourier-transform infrared spectroscopy (FT-IR; ALPHA, Bruker, Billerica, MA, USA) and X-ray photoelectron spectroscopy (XPS; PHI GENESIS 500, ULVAC Phi Co., Ltd., Kanagawa, Japan). The Zeta potentials of the membrane surfaces were measured with a SurPASS™ 3 electrokinetic analyzer (Anton Paar GmbH, Graz, Austria). Matrix-assisted laser desorption/ionization (MALDI, MALDI-8020, Shimadzu Co., Kyoto, Japan) was used to measure molecular-mass leakage. UV–Vis (UV3600, Shimadzu) spectra were obtained to measure MO and NICA concentrations. Liquid chromatography mass spectrometry (LCMS, LCMS-8045, Shimadzu Co.) was used to estimate PPG concentration.

For swelling tests, membranes were prepared by vacuum-assisted IP at the AAO substrate and immersed in 20 mL MeOH or DMSO for 24 h. For SEM and AFM images, the membrane samples were kept at −80 °C and freeze-dried for three days. For mass spectral investigation of oligomer leaching, 10 mL above solutions were concentrated by freeze-drying to 0.5 mL. Then, 1 μL of the solution was mixed with 1 μL of 0.1 % aqueous trifluoroacetic anhydride solution, and the mixture was freeze-dried for 24 h.

2.5. Evaluation of membrane performance

Membrane performances were evaluated using a crossflow filtration system. The effective membrane area was 7.07 cm^2, the flow rate of the feed was 10.0 mL min^{-1}, and the applied pressure was 10 bar. The feed solution side of the membrane cell was stirred at ~600 rpm to prevent concentration polarization. After a fixed time (at least 2 h) of continuous operation, the stable solvent permeance was estimated from the mass changes in the permeate. Then, MO was evaluated after a continued operation of 2 h using dye solutions with a concentration of 50 ppm. The concentrations of dyes in solutions were measured by UV–Vis spectroscopy. The membrane pore size was estimated based on PPG rejection in MeOH and DMSO (1000 ppm, including 1188 g solvent, 4 g PPG 400, 4 g PPG 800, and 4 g PPG 1000). The concentrations of the feed and permeate were diluted 200 times with 0.1 v% formic acid/acetonitrile solution and calculated from the LCMS spectra area.

The solvent permeance (J_V, L m^{-2} h^{-1} bar^{-1} = LMH/bar) and dye rejection (R, %) were calculated using Eqs. (1) and (2):

$$J_V = \frac{V}{T \times A \times P} \tag{1}$$

where *V, A, T,* and *P* are the permeate volume (L), effective membrane area (m^2), operation time (h), and transmembrane pressure (bar), respectively, and:

$$R\ (\%) = \left(1 - \frac{C_p}{C_f}\right) \times 100 \tag{2}$$

where C_p and C_f are the solute concentrations of the permeate and feed solutions, respectively.

The MWCO of the membrane was estimated from molecular weight with 90 % PPG rejection in MeOH or DMSO in the MWCO curve, and the pore size was estimated by applying the relationship between the molecular weight (M) of the neutral molecules and the Stokes diameter (d_p, nm) in Eq. (3) [31]:

$$d_p = 33.46 \times 10^{-12} \times M^{0.557} \tag{3}$$

3. Results and discussion

3.1. Characterization of membranes

As illustrated in Fig. 1a, this porphyrin-based bridge is inspired by the feature of *heme*-catalyzed oxygen carrier processes [26,28,32]. In a typical oxygen reduction part, the coordination between (TAPP)Fe(II) and O_2 from air forms a π-bond and triggers electron transfer from the Fe *d*-orbital to the empty O π* orbital to yield (TAPP)Fe(III)–O_2*. This unpaired electron will connect with an additional (TAPP)Fe(II) to form (TAPP)Fe(III)–O_2–Fe(III)(TAPP). The active O^--O^- further oxidizes Fe (III), and homolytic cleavage leads to (TAPP)Fe(IV)═O. This oxidative compound finally reacts with (TAPP)Fe(II) to generate the stable (TAPP)Fe(III)–*O*–Fe(III)(TAPP). This mechanism is corroborated by the emergence of Fe–*O*–Fe bridges, as evidenced by oxygen-containing bond formation and the oxidation state evolution of (TAPP)Fe(II).

To demonstrate successful formation of the porphyrin network and Fe^{2+} integration into the selective layer, a TAPP-IPC membrane was fabricated on an AAO substrate via vacuum-assisted IP. Defect-free membrane morphology was confirmed by digital photography (Fig. 2a). Subsequent Fe^{2+} post-treatment (65 °C, 20 h) yielded an Fe-TAPP-IPC membrane, with cross-sectional SEM-EDS revealing pronounced C and Fe enrichment at the surface, distinct from the Al signal of the substrate (Figs. S1–S2). Notably, Fe-TAPP-IPC exhibits higher Fe intensity and uniform distribution compared with pristine TAPP-IPC, preliminarily confirming the porphyrin-Fe assembly. The ATR-IR spectra (Fig. 2b) further verified polycondensation between TAPP and IPC, with characteristic peaks at 1680 cm^{-1} (C═O, amide), 1592 cm^{-1}

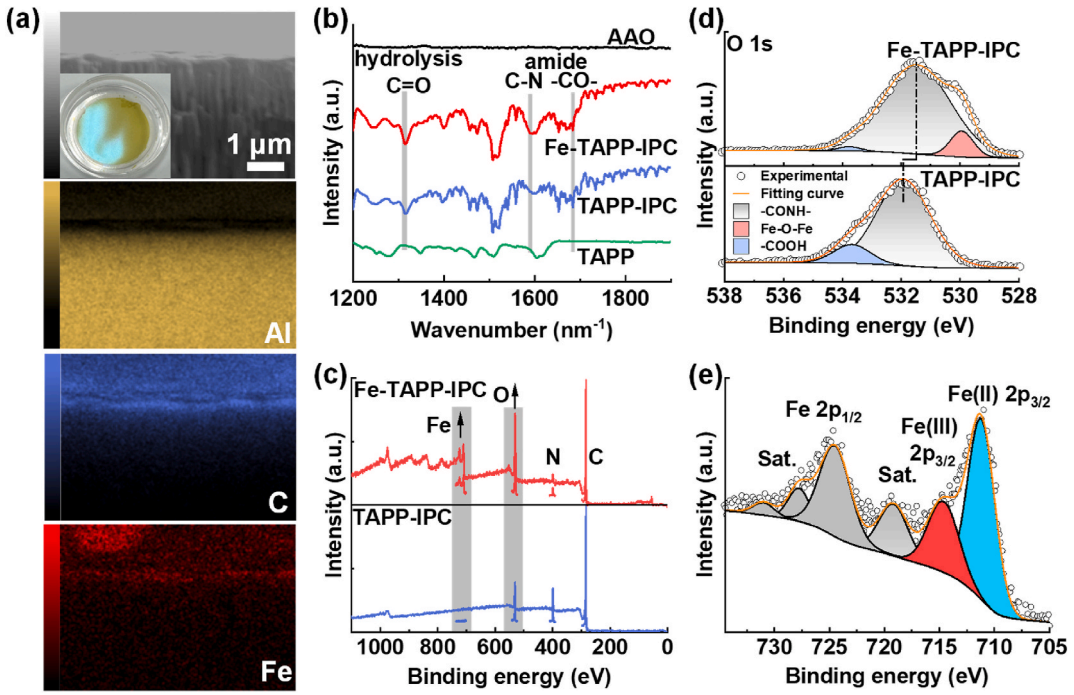

Fig. 2. a) Cross-section and EDS images of Fe-TAPP-IPC and (inset) digital photograph of the membrane formed at the AAO substrate (diameter: 47 mm). b) ATR-FTIR and c) wide spectra of TAPP-IPC and Fe-TAPP-IPC. d) O 1s XPS spectra of TAPP-IPC and Fe-TAPP-IPC, and e) Fe 2p spectrum of Fe-TAPP-IPC.

(C–N), and 1315 cm^{-1} (C═O, –COOH from unreacted hydrolyzed acyl chloride) [32]. The spectral similarity between TAPP-IPC and Fe-TAPP-IPC confirms the preservation of the porphyrin network during Fe incorporation [11].

XPS was employed to explore structural change after Fe incorporation. In the wide scan (Fig. 2c), the surface modification resulted in increased Fe amount (9.5 %) and O/C ratio from 0.118 to 0.323 in Fe-TAPP-IPC compared with pristine TAPP-IPC. For the narrow O spectra of the pristine TAPP-IPC (Fig. 2d), the spectra can be deconvoluted into signals for an amide bond at 532.2 eV (N–C═O, 84.9 %) and a carboxylic acid group at 534.1 eV (O–C═O, 15.1 %) because all the oxygen is derived from IPC. Based on the '4 + 2' topological connection, TAPP-IPC is regarded as a two-dimensional network without interlayer bridges [33,34]. Fe-TAPP-IPC exhibits a new shoulder peak at 529.8 eV (13.2 %), which is consistent with the metal-O bond energy established in previous work [35]. Furthermore, there is a potential coordination bond between –COOH and Fe ions formed by electrostatic attraction with relatively low intensity for the carboxylic acid group (3.7 %), which leads to a negative shift of the main peak from 531.9 to 531.6 eV [18,36]. The high-resolution XPS Fe 2p spectra (Fig. 2e) feature $2p_{1/2}$ (724.9 eV) and satellite peaks (718.9, 728.5, and 731.4 eV). Critically, the $2p_{3/2}$ region is fitted to Fe(II) (711.1 eV, 36.4 %) and Fe(III) (714.2 eV, 18.7 %), consistent with our hypothesis, i.e., that Fe^{2+} not only coordinates within porphyrin centers but also undergoes O_2-mediated oxidation to form inter-network Fe–*O*–Fe bridges. According to Zeta potential measurement, the negative charge of Fe-TAPP-IPC is lower than those of TAPP-IPC and the substrate because the effect of COOH is weakened by cross-linking with Fe (Fig. S3).

3.2. *Effect of DMSO on swelling*

Previous studies have employed DMSO as an activation agent to enhance the permeance of PA membranes at the cost of selectivity [20,21]. This trade-off arises from DMSO's high polarity (compared with DMF and NMP), which facilitates the dissolution of low molecular weight oligomers and increases PA-segment mobility, thereby altering membrane morphology. However, a high activation degree implies an inherent instability of PA membranes in DMSO.

To evaluate DMSO-induced structural changes, membranes were immersed in DMSO for 24 h, freeze-dried, and examined by SEM (Fig. 3ab). The conventional PA membrane MPD-TMC, fabricated via IP, exhibits a rough, crumpled morphology above the substrate, with ridge regions swelling into micro-sized nodules upon activation. In contrast, the TAPP-IPC and Fe-TAPP-IPC membranes show smooth surfaces before and after activation, demonstrating their superior stability. Furthermore, no metal aggregates are observed on the surface of Fe-TAPP-IPC, indicating that Fe is not introduced as nanoparticles, but rather as a highly dispersed atomic Fe species [16,37]. The crumpling of MPD-TMC is due to the mold interface, with the conventional IP process limited to the inner region of the porous substrate, so it is susceptible to fluctuations due to exothermic reactions or produced bubbles [38,39]. These significant differences may initially be attributed to the IP process. The uneven swelling of the collapsed ridges at the underlying porous substrate can cause detachment of the selective layer [40].

The swelling effects are also examined by their intrinsic thickness changes. By using the vacuum-assisted IP, MPD-TMC exhibited a smooth surface due to the stable monomer concentration and limited local temperature changes, which is similar to the porphyrin networks to exclude the effect of membrane fabrication method (Fig. S4). Furthermore, MPD-TMC, TAPP-IPC, and Fe-TAPP-IPC exhibit activated thicknesses of 33, 67, and 70 nm by using AFM, which are 2.2, 1.5, and 1.2 times their pristine thicknesses. The lower degree of change in the porphyrin membranes indicates that the polyaromatic building block is instrumental to membrane stability. The removal of low molecular weight oligomers by DMSO is supposed to dominate the membrane activation behavior over solvent swelling of the selective layer. The thickness of Fe-TAPP-IPC is lower than that of TAPP-IPC, while those of their activated membranes are similar, which is attributed to the fact that DMSO removes unreacted TAPP monomers, and the selective layer shows no structural collapse during post-treatment and DMSO activation [41].

To demonstrate the stabilizing effect of Fe modification on porphyrin-based membranes, we conducted mass sepectra analysis of the dissolved fragments in three leach solutions: TAPP-IPC in methanol,

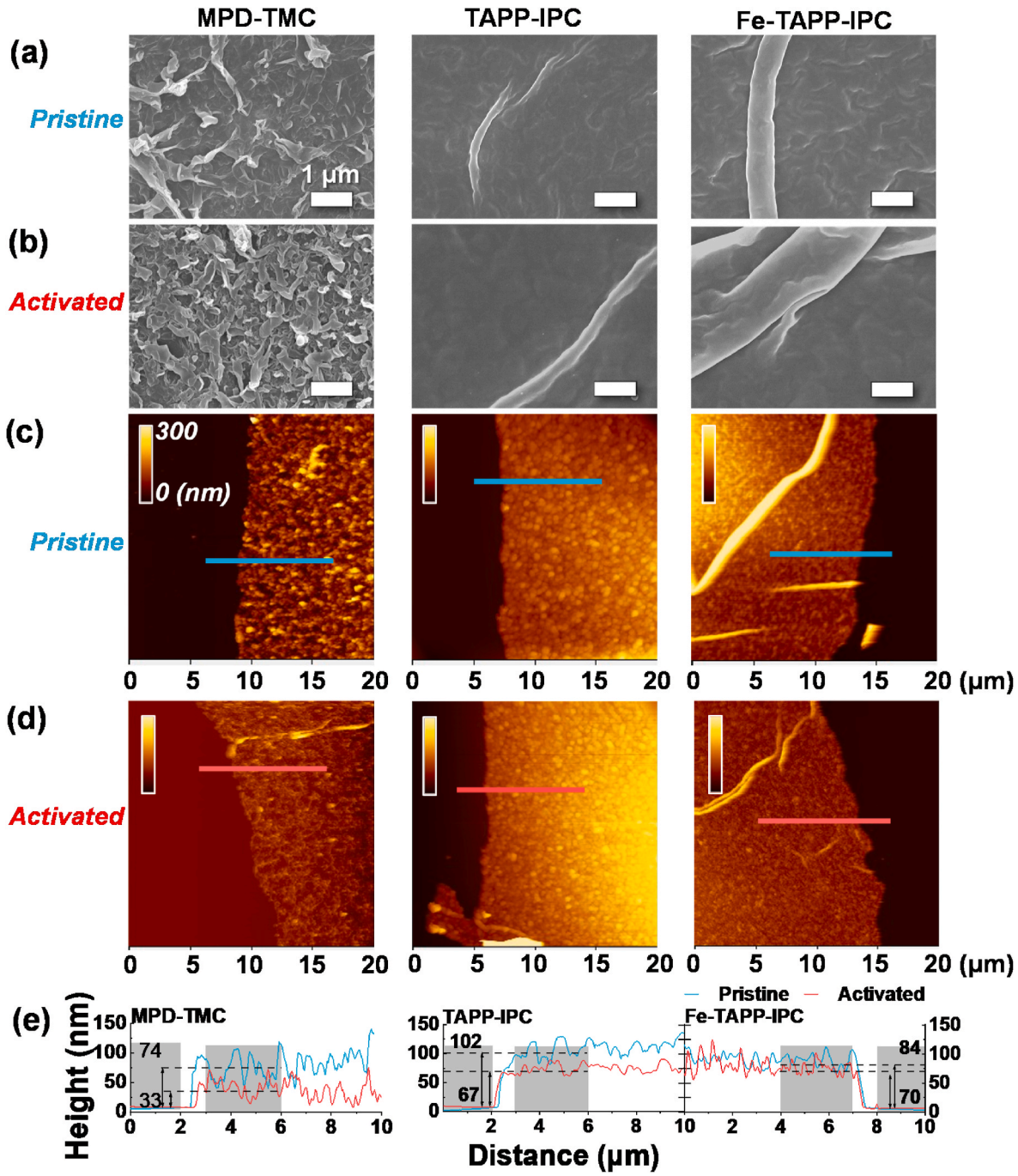

Fig. 3. Freeze-dried surface morphologies of MPD-TMC, TAPP-IPC, and Fe-TAPP-IPC (a) before and (b) after 24 h DMSO activation with a scale bar of 1 μm. Corresponding AFM topography images with a height scale of 300 nm (c) before and (d) after 24 h DMSO activation and (e) membrane thickness changes derived from the above AFM images.

TAPP-IPC in DMSO, and Fe-TAPP-IPC in DMSO (Fig. 4). The spectral peak areas and molecular weight correlate directly with the solubilities of the membrane fragments, providing quantitative insight into structural stability. TAPP-IPC series exhibit characteristic peaks at ~675 Da, corresponding to the TAPP monomer, with maximum value below 2000 Da. DMSO has higher solubility to TAPP-IPC than MeOH, as shown by the higher intensity and largest molecular fragment at the mass spectra, which are close to 'TAPP+3IPC' (1143.06 Da) and '2TAPP+3IPC' (1819.77 Da). Fe-TAPP-IPC presents a peak for 'Fe-TAPP-2IPC' at 1083.73 Da, which is lower in intensity than that for the unmodified counterpart, indicating reduced solubility and thus improved network stability. This is consistent with the observed morphology changes. In comparison, the oligomer of MPD-TMC in MeOH and DMSO has a similar tendency but exhibits intensities that is 2–3 orders of magnitude stronger than that of TAPP-IPC in a wide molecular weight range (~6000 Da) (Fig. S5). It is consistent with the reported oligomer weight, and further confirms that the larger polyaromatic structure of TAPP-IPC contributes significantly to the enhanced stability of the membrane [11, 42].

To exclude the effect of the chloride monomer on membrane morphologies and swelling behavior in TAPP-IPC and MPD-TMC, TMC was also used to form TAPP-TMC and Fe-TAPP-TMC. The XPS results for TAPP-TMC show a higher amide ratio than that for TAPP-IPC, and the Fe–*O*–Fe is also introduced to the porphyrin (Fig. S6). Because TMC has

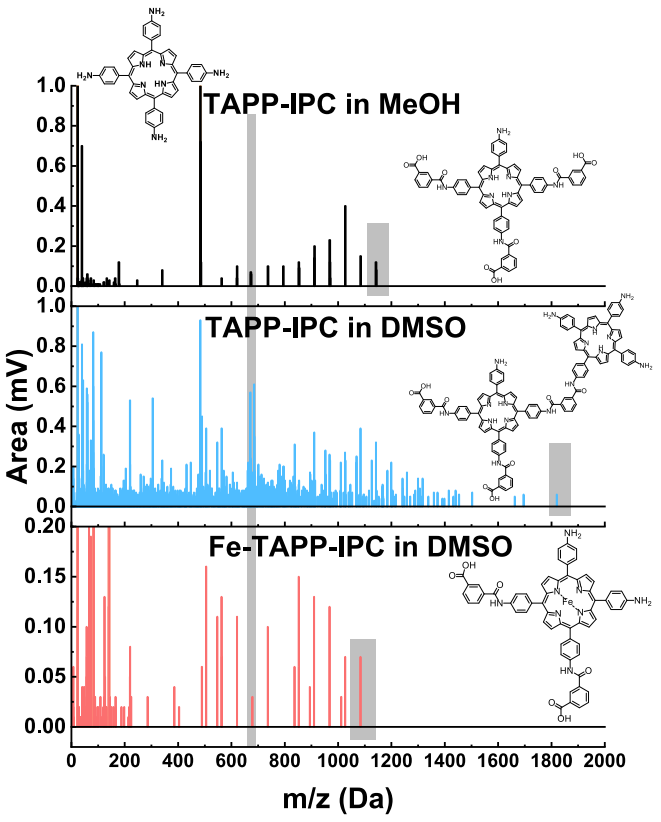

Fig. 4. MALDI-MS spectra showing the molecular weight of leached oligomers with inset images of the corresponding molecules.

aryl chlorides at the same position as IPC and has an additional one, the former amide bonds were separated into an in-plane network connection and an additional interlayer amide bridge. Besides the similar surface changes and oligomer leaching observed in Figs. S7 and S8, the formation of the thinner pristine selective layer (19 nm) indicates that the difference in membrane thickness can be attributed to the highly connected chlorides. The DMSO activation causes a converse change in TAPP-TMC, with a layer thickness of 25 nm, which indicates significant swelling behavior for the amide, and establishes a stability rank in DMSO that follows MPD-TMC < TAPP-TMC < TAPP-IPC < Fe-TAPP-IPC ~ Fe-TAPP-TMC.

3.3. Separation performance change

To evaluate the effect of the Fe–*O*–Fe bridge on membrane stability, four typical membranes were prepared for comparison: TAPP-IPC (without Fe post-treatment) and Fe-TAPP-IPC, conventional MPD-TMC, and Fe-MPD-TMC (with the same Fe post-treatment and no porphyrin unit) and the permeance changes were compared using a continuous MeOH/DMSO/MeOH filtration cycle (Fig. 5a).

First, pristine MPD-TMC and TAPP-TMC show similar developments throughout the process: at stage I, their permeance decline indicates membrane compaction to a stable state. At stage II, the DMSO permeances of MPD-TMC and TAPP-IPC are 11- and 3.1-fold, respectively, those for MeOH. At stage III, the activated membranes show slower declines during the 12 h operation, but still higher than stable MeOH permeance. Considering the higher viscosity (η) of DMSO than that of MeOH, this higher DMSO permeance and the changes demonstrate unwanted structural flexibility. The smaller change for TAPP-IPC indicates that the polyaromatic ring contributes to a stable structure, but not sufficiently.

Next, the DMSO permeance of Fe-TAPP-IPC is 0.38 times the MeOH permeance at stage II, and it shows stable MeOH permeance at stage III. This converse tendency demonstrates that the stability of the porphyrin network is enhanced by the Fe–*O*–Fe bridging, allowing it to resist DMSO swelling. In comparison to Fe-MPD-TMC, this method was further proved to be established at porphyrin. Fe-MPD-TMC has the same DMSO permeance as MPD-TMC, while its MeOH permeance is 10 times higher than the latter, indicating that the swelled network formed during the post-treatment.

More importantly, because of the fine solutes typically addressed in nanofiltration (200–1000 Da), the rejection of MO (327 Da, 0.5 × 1.5 nm) in solutions was investigated at the end of stage II by UV–Vis absorbance (Fig. 5b). Consistent with the DMSO permeance, the absorbance follows the order of Fe-MPD-TMC > MPD-TMC > TAPP-IPC ≫ Fe-TAPP-IPC. Therefore, both the porphyrin network and Fe–*O*–Fe crosslinks are indispensable for stable membrane performance.

Furthermore, the permeances of mildly polar solvents for Fe-TAPP-IPC, including MeOH, EtOH, 1-propanol and 1-butanol, was analyzed in terms of solvent viscosity (η), molecule size (d_m) and solvent parameter referring to the polarity δ_p) according to solution-diffusion theory and compared with those for DMSO (Table S1) [43–45]. As shown in Fig. 5c and S9, Fe-TAPP-IPC exhibits a better correlation for $\delta_p \cdot \eta^{-1}$ than η^{-1} and $\delta_p \cdot \eta^{-1} d_m^{-2}$, indicating that the solvent transport mainly follows viscous continuum flow in nanopores and is affected by the polarity interaction between pore wall and solvent. Regarding the permeance difference between DMSO and MeOH for TAPP-IPC, the swelling effect of the polar aprotic solvent on the porphyrin network of Fe-TAPP-IPC is significantly reduced, whereby DMSO permeance corresponds to the fitting line.

For initial optimization, the conditions for $FeCl_2$ post-treatment, including concentration, reaction temperature, and time, were explored. When those factors surpass each of their threshold values (8.125 mg mL^{-1}, 65 °C, and 5 h), membrane stability increases with each value increasing, judged by the decreased DMSO permeance and increased MO rejection (Fig. S10). Further exploration was based on a different set of membrane-forming conditions (65 °C, 0.128 mmol mL^{-1}, and 20 h) with DMSO stability and higher permeance. Fig. 5d and e compares the separation performances of the porphyrin and conventional membranes to highlight their characteristics. At stage I, Fe-MPD-TMC and Fe-TAPP-IPC show MeOH permeances of 11.7 and 4.6 LMH/bar, which are higher than those of pristine MPD-TMC and TAPP-IPC (1.0 and 1.5 LMH/bar), and these results are consistent with their membrane thickness changes. At stage II, only Fe-TAPP-IPC achieves efficient MO rejection (96.2 %) with a low DMSO permeance of 1.5 LMH/bar. TAPP-IPC, MPD-TMC and Fe-MPD-TMC show the MO rejections of 34.0, 21.1 and 17.3 % in turn, despite their high DMSO permeances. At stage III, the irreversible cleaning of DMSO and the membrane compaction led to improved MeOH permeances and MO rejections in MPD-TMC (2.9 LMH/bar, 98.6 %) and TAPP-IPC (2.4 LMH/bar, 83.1 %). In comparison, Fe-MPD-IPC (9.4 LMH/bar, 95.1 %) and Fe-TAPP-IPC (4.6 LMH/bar, 95.1 %) exhibited the various structure compaction followed by the post-treatment in DMSO.

Combining the performance changes in stage II-III, MPD-TMC series is suitable for mild alcohol, because it has no structure collapse after DMSO activation, thereby achieving a higher permeance with a slight MO rejection decline in MeOH. But, considering the applications of industrial operation using polar porotic solvents, Fe-TAPP-IPC demonstrates the outstanding potential of solvent resistance and structure recovery due to the stable MO rejection (>95 %) and solvent permeance, which is similar to the reported integrally skinned asymmetric membranes without a complex membrane fabrication process (Table S2).

The pore sizes of porphyrin membranes were evaluated using neutral PPG molecules as probes, since dye rejection can be affected by differences in aggregation and charge states in solvents [3]. As seen from the liquid chromatograms of the feed and permeate samples, Fe-TAPP-IPC removes most of the PPG from DMSO, especially molecular weight above 354 Da (n = 6) (Fig. 6a). Their MWCO curves show (rejection = 90 %) a reversible tendency (Fig. 6b). TAPP-IPC shows a marked shift

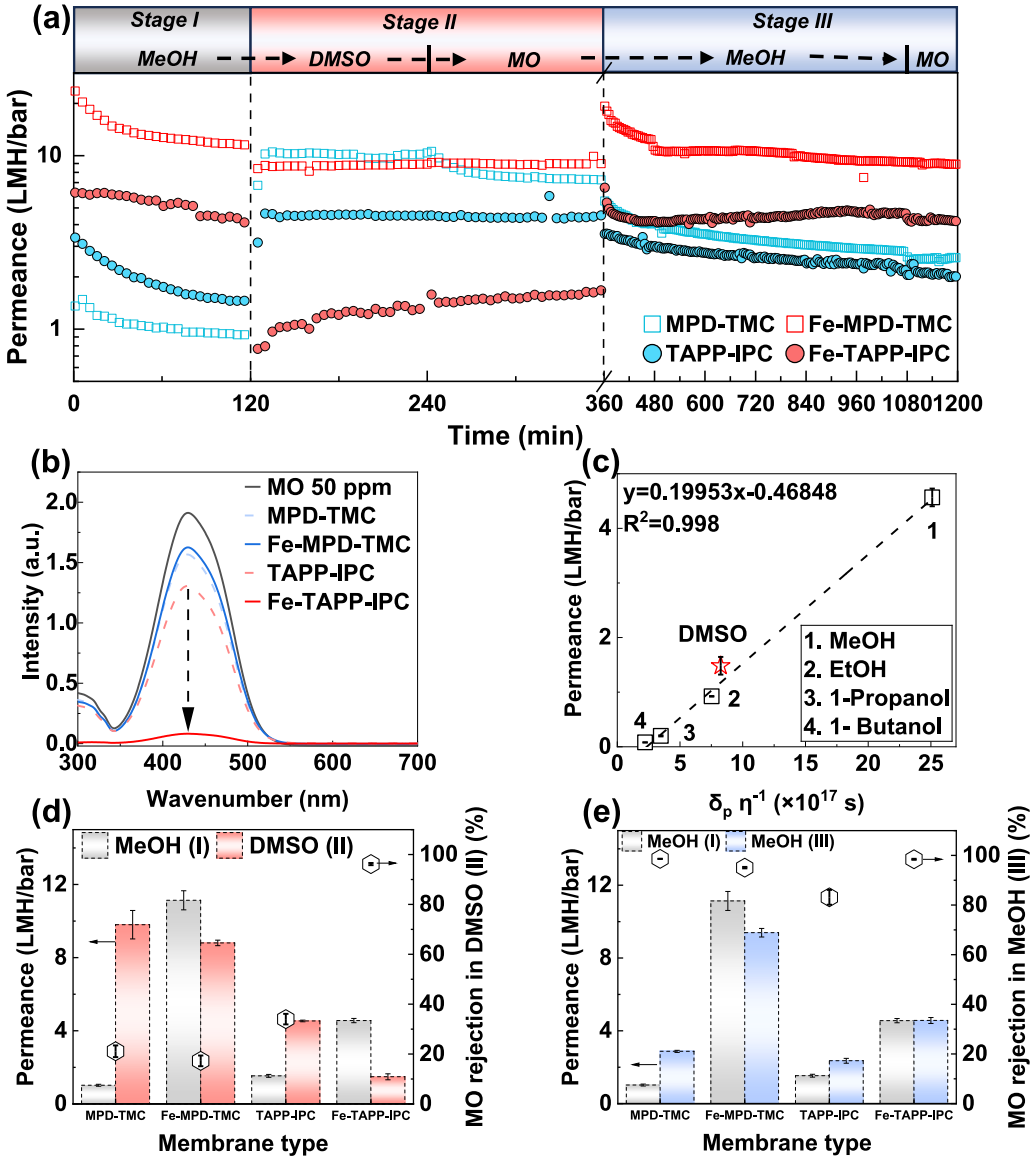

Fig. 5. a) Time development of membrane permanence in nanofiltration tests with three stages, including stage I: MeOH (2 h), stage II: DMSO (2 h), MO/DMSO (2 h), and stage III: MeOH (12 h), and MO/MeOH (2 h). b) UV–Vis spectra of DMSO solutions to calculate MO (327 Da) rejection. c) Solvent permeance of the Fe-TAPP-IPC membrane, which correlates with the combined solvent property (δ_p: Hansen solubility parameter arising from the dipole force, and η: viscosity) and comparison of solvent permeance and MO rejection between (d) stages I and II, and (e) stages I and III.

between 450 and 1180 Da and achieves a lower MWCO of 420 Da in stage III, which can probably be attributed to DMSO purifying the porphyrin network by removal of low molecular weight oligomers. In comparison, Fe-TAPP-IPC has a durable structure, and thus only a slight MWCO change between 360 and 420 Da.

For their pore sizes changes in TAPP-IPC and Fe-TAPP-IPC, using the relationship between molecular weight and Stokes diameter, the above cut-off sizes were calculated to be 0.89 (360 Da) < 0.97 (420 Da) < 1.00 (450 Da) < 1.72 nm (1180 Da), which are in accordance with offset stacked and single-layer porphyrin networks [31]. Similar to two-dimensional graphene oxide laminate, the swelling behavior was mainly caused by increasing the distance of the porphyrin units, which leads to failure of the stacking effect, as shown in Fig. 5a, stage II. Through the formation of Fe–*O*–Fe bridges, the stability was enhanced [46,47].

As the additional comparison, MPD-TMC and TAPP-TMC series were also examined to further confirm the effect of porphyrin and Fe–*O*–Fe bridge (Fig. S11), the former exhibited more dramatic changes for the MeOH-DMSO cycle over the PPG molecular scale, and the post-treatment in DMSO further eroded the membrane fragment due to the lack of porphyrin units, resulting in a loose Fe-MPD-TMC membrane. The latter was regarded as the two-dimensional network with the interlayer amide bond. It has MWCO in DMSO above 1300 Da and this shift was also stabilized by the Fe–*O*–Fe bond to demonstrate higher robustness than the amide bond. This exceptional trend between TAPP-TMC and TAPP-IPC is consistent with the above thickness changes and the theory discussed above, the amide linkage's higher susceptibility to DMSO seems to make it a detriment to SRNF performance [19].

We investigated the industrial potential of the membranes for the treatment of active pharmaceutical intermediates in long-term operation (Fig. 6c and d). To exhibit the sensitivity for low-weight molecules, Fe-TAPP-IPC was employed for the recovery of the Cefixime intermediate NICA (259 Da, 0.97 × 1.43 nm) [48]. Due to the low oligomer removal during 7 days of continuous filtration, DMSO permeance increases from 1.4 to 2.6 LMH/bar without severe NICA rejection decline (Rejection >96.7 %) (Fig. 6d). In particular, when the membrane was

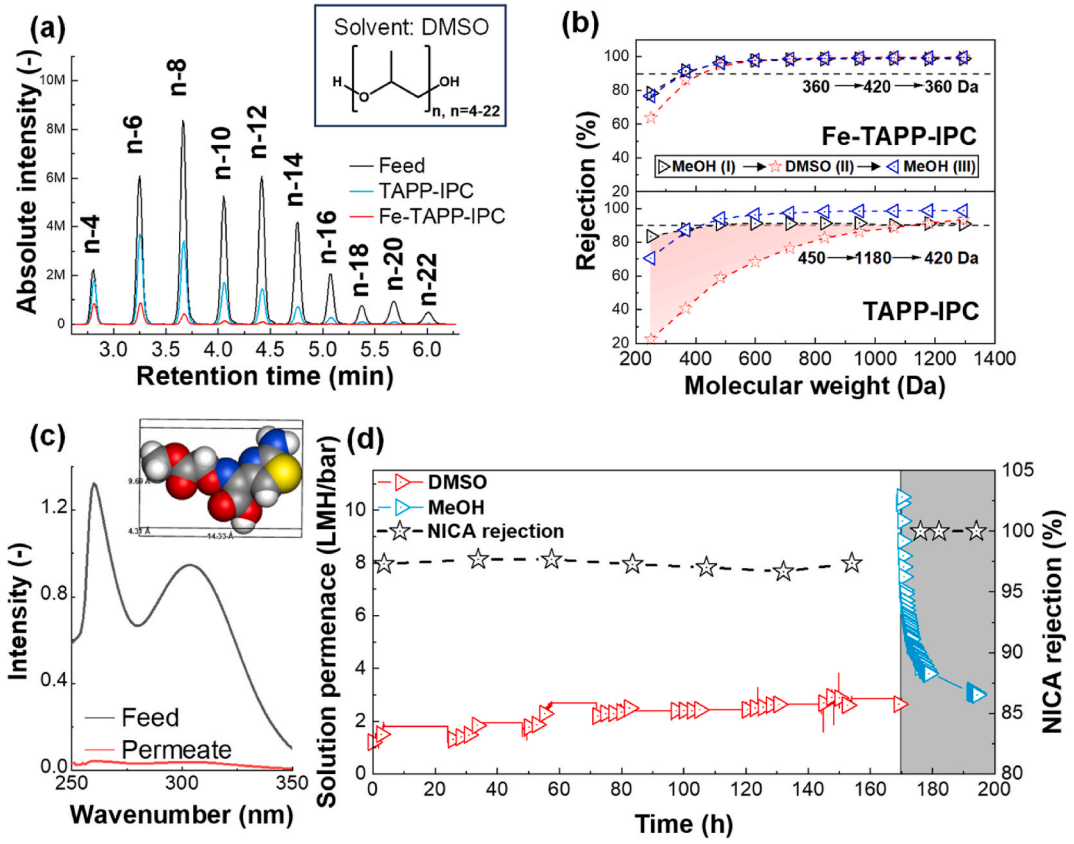

Fig. 6. a) Chromatogram of mixed PPG solutions from LCMS analysis and corresponding PPG molecule weight to exhibit the rejection of TAPP-IPC and Fe-TAPP-IPC membranes in DMSO. b) MWCO changes in TAPP-IPC and Fe-TAPP-IPC at the three stages. c) UV–Vis spectra of NICA/DMSO solutions (inset shows the NICA formula. d) Long-term continuous operation of Fe-TAPP-IPC for 168 h in DMSO and 24 h MeOH.

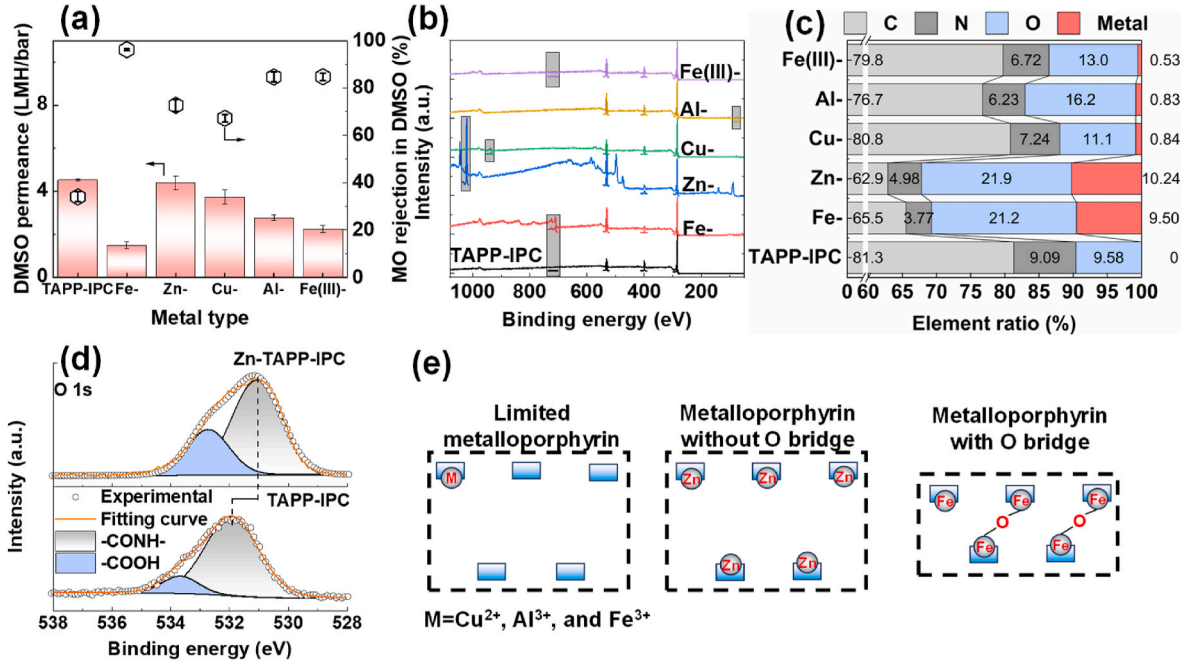

Fig. 7. a) The relationship between separation performance in DMSO and metal ions in modified TAPP-IPC membranes. b) Wide spectra and c) elemental ratios for TAPP-IPC membranes under various metal ion modifications. d) O 1s spectra of Zn-TAPP-IPC and TAPP-IPC. e) Illustration of the three possible structures in metal-TAPP-IPC membranes.

re-compacted using MeOH, total recovery of NICA (>99 %) was accomplished.

3.4. Specificity of Fe–O–Fe bridge

Finally, the method was applied using other metal ions at the same molar concentration. According to hard-soft acid-base theory, divalent Cu^{2+} and Zn^{2+} were chosen because of their high solvent stability, and trivalent Fe^{3+} and Al^{3+} were used to further examine the effect of oxidation of Fe(II) [18]. Comparing their DMSO permeances and MO rejections, Cu- (3.7 LMH/bar, 67.2 %) and Zn-TAPP-IPC (4.2 LMH/bar, 72.7 %) show the lowest porphyrin stabilization, and those for Fe(III)- (2.1 LMH/bar, 84.8 %) and Al-TAPP-IPC (2.8 LMH/bar, 84.6 %) are also limited (Fig. 7a).

Combining the XPS results (Fig. 7b and c), the metal ratio of the modified membranes decreases in the order Zn^{2+} (10.2 %) > Fe^{2+} (9.5 %) ≫ Cu^{2+} (0.8 %) ~ Al^{3+} (0.8 %) ~ Fe^{3+} (0.5 %) in wide-scan spectra. The poor SRNF performance may be attributed to the limited metal ratios incorporated in the membrane for Cu^{2+}, Al^{3+}, and Fe^{3+}. This may be further explained in terms of the kinetic formation of metalloporphyrins with metal type: that for Cu^{2+} has a high equilibrium constant, so it easily escapes from the porphyrin center under filtration-like operation to recover the TAPP-IPC state [49,50]. However, coordination of Fe^{3+} and Al^{3+}, accompanied by porphyrin deformation, is more difficult (but irreversible) than that of the other metals [51]. Compared with Zn^{2+} and Fe^{2+} with similar ratios in metal and O (Figs. 2d and 7d), the former presents an amide (531.1 eV, 70.0 %) and carboxylic acid group (532.7 eV, 30.0 %). Thus, the above metal ions generate three kinds of porphyrin structure (Fig. 7e), demonstrating the importance of the metalloporphyrin and redox reaction with oxygen. Even if this bridge is unique to Fe ions, similar reactions have been widely studied in *N*-containing molecules and redox metals to further promote membrane design [32,52,53].

4. Conclusions

In summary, we have successfully demonstrated the generation of an Fe–*O*–Fe-bridged porphyrin network for the solvent-resistant nanofiltration, prepared with a facile interlayer polymerization and post-treatment process. The stability of porphyrin and this coordination bond in variable and complex solvents was systematically confirmed by the structural and separation performance changes in MeOH and DMSO. Contributed to the highly conjugated rings, the porphyrin-based membranes reveal the minimized solubility in polar solvents, due to the lowest oligomer leaching and morphology changes in DMSO. By applying this method to the conventional polyamide (MPD-TMC) and other metal ions (Cu, Zn, Al and Fe(III)), the key to the stable polyamide is proven to the coordination site of the porphyrin center and the redox Fe bridge construction process. Therefore, the final Fe-TAPP-IPC exhibited stable DMSO permeance, rejection for fine solute of MO above 95.6 %, and minimized MWCO shift (between 360 and 420 Da). In long-term filtration, it also showed efficient recovery of NICA in DMSO over 7 days. Conceivably, our crosslinking strategy shows a novel insight for preparing effective SRNF membranes.

CRediT authorship contribution statement

Zheng Wang: Writing – original draft, Visualization, Validation, Methodology, Investigation, Formal analysis. **Keizo Nakagawa:** Writing – review & editing, Project administration, Methodology, Funding acquisition, Conceptualization. **Kecheng Guan:** Writing – review & editing, Methodology. **Aiwen Zhang:** Writing – review & editing, Methodology. **Yasunao Okamoto:** Investigation. **Atsushi Matsuoka:** Investigation. **Eiji Kamio:** Writing – review & editing. **Tomohisa Yoshioka:** Writing – review & editing, Software, Investigation. **Hideto Matsuyama:** Writing – review & editing, Supervision, Project administration, Funding acquisition.

Declaration of competing interest

The authors declare the following financial interests/personal relationships which may be considered as potential competing interests: Hideto Matsuyama is an Editor of the journal but was not involved in the paper review or handling of this paper.

Acknowledgments

This work was supported by JSPS KAKENHI Grant Number JP25K01563.

Appendix. ASupplementary data

Supplementary data to this article can be found online at https://doi.org/10.1016/j.memsci.2025.124485.

Data availability

Data will be made available on request.

References

[1] P. Marchetti, M.F. Jimenez Solomon, G. Szekely, A.G. Livingston, Molecular separation with organic solvent nanofiltration: a critical review, Chem. Rev. 114 (21) (2014) 10735–10806, https://doi.org/10.1021/cr500006j.
[2] S.L. Aristizábal, R.P. Lively, S.P. Nunes, Solvent and thermally stable polymeric membranes for liquid molecular separations: recent advances, challenges, and perspectives, J. Membr. Sci. 685 (2023) 121972, https://doi.org/10.1016/j.memsci.2023.121972.
[3] R. Verbeke, I. Nulens, M. Thijs, M. Lenaerts, M. Bastin, C. Van Goethem, G. Koeckelberghs, I.F.J. Vankelecom, Solutes in solvent resistant and solvent tolerant nanofiltration: how molecular interactions impact membrane rejection, J. Membr. Sci. 677 (2023) 121595, https://doi.org/10.1016/j.memsci.2023.121595.
[4] D.R. Flores, D.L. Shaffer, Quantifying steric, non-steric, and adsorption contributions to solute rejection in covalent organic framework nanofiltration membranes, J. Membr. Sci. 715 (2025) 123491, https://doi.org/10.1016/j.memsci.2024.123491.
[5] D. Zhao, J.F. Kim, G. Ignacz, P. Pogany, Y.M. Lee, G. Szekely, Bio-inspired robust membranes nanoengineered from interpenetrating polymer networks of polybenzimidazole/polydopamine, ACS Nano 13 (1) (2019) 125–133, https://doi.org/10.1021/acsnano.8b04123.
[6] F. Gao, R. Bai, F. Ferlin, L. Vaccaro, M. Li, Y. Gu, Replacement strategies for non-green dipolar aprotic solvents, Green Chem. 22 (19) (2020) 6240–6257, https://doi.org/10.1039/D0GC02149K.
[7] X. He, A. Zhou, C. Shi, J. Zhang, W. Li, Solvent resistant nanofiltration membranes using EDA-XDA co-crosslinked poly(ether imide), Sep. Purif. Technol. 206 (2018) 247–255, https://doi.org/10.1016/j.seppur.2018.05.031.
[8] W. Xie, T. Li, A. Tiraferri, E. Drioli, A. Figoli, J.C. Crittenden, B. Liu, Toward the next generation of sustainable membranes from green chemistry principles, ACS Sustain. Chem. Eng. 9 (1) (2021) 50–75, https://doi.org/10.1021/acssuschemeng.0c07119.
[9] A.M. Shenoy, R. Thür, B. van Duffel, I.F.J. Vankelecom, Use of green polar aprotic solvents TamiSolve® NxG, DMSO and methyl-THF for the synthesis of asymmetric polyimide-based biogas purification membranes, J. Membr. Sci. 717 (2025) 123573, https://doi.org/10.1016/j.memsci.2024.123573.
[10] M.F. Jimenez Solomon, Y. Bhole, A.G. Livingston, High flux membranes for organic solvent nanofiltration (OSN)—Interfacial polymerization with solvent activation, J. Membr. Sci. 423–424 (2012) 371–382, https://doi.org/10.1016/j.memsci.2012.08.030.
[11] M.G. Shin, J.Y. Seo, H. Park, Y.-I. Park, J.-H. Lee, Overcoming the permeability-selectivity trade-off of desalination membranes via controlled solvent activation, J. Membr. Sci. 620 (2021) 118870, https://doi.org/10.1016/j.memsci.2020.118870.
[12] A. Asadi Tashvigh, Y. Feng, M. Weber, C. Maletzko, T.-S. Chung, 110th anniversary: selection of cross-linkers and cross-linking procedures for the fabrication of solvent-resistant nanofiltration membranes: a review, Ind. Eng. Chem. Res. 58 (25) (2019) 10678–10691, https://doi.org/10.1021/acs.iecr.9b02408.
[13] I.B. Valtcheva, S.C. Kumbharkar, J.F. Kim, Y. Bhole, A.G. Livingston, Beyond polyimide: crosslinked polybenzimidazole membranes for organic solvent nanofiltration (OSN) in harsh environments, J. Membr. Sci. 457 (2014) 62–72, https://doi.org/10.1016/j.memsci.2013.12.069.
[14] K. Vanherck, A. Cano-Odena, G. Koeckelberghs, T. Dedroog, I. Vankelecom, A simplified diamine crosslinking method for PI nanofiltration membranes,

J. Membr. Sci. 353 (1) (2010) 135–143, https://doi.org/10.1016/j.memsci.2010.02.046.
[15] A. Asadi Tashvigh, L. Luo, T.-S. Chung, M. Weber, C. Maletzko, Performance enhancement in organic solvent nanofiltration by double crosslinking technique using sulfonated polyphenylsulfone (sPPSU) and polybenzimidazole (PBI), J. Membr. Sci. 551 (2018) 204–213, https://doi.org/10.1016/j.memsci.2018.01.047.
[16] R. Hardian, P. Pogany, Y.M. Lee, G. Szekely, Molecular sieving using metal–polymer coordination membranes in organic media, J. Mater. Chem. A 9 (25) (2021) 14400–14410, https://doi.org/10.1039/D1TA02601A.
[17] J. Hu, R. Hardian, M. Gede, T. Holtzl, G. Szekely, Reversible crosslinking of polybenzimidazole-based organic solvent nanofiltration membranes using difunctional organic acids: toward sustainable crosslinking approaches, J. Membr. Sci. 648 (2022) 120383, https://doi.org/10.1016/j.memsci.2022.120383.
[18] X. Luo, Z. Wang, S. Wu, W. Fang, J. Jin, Metal ion cross-linked nanoporous polymeric membranes with improved organic solvent resistance for molecular separation, J. Membr. Sci. 621 (2021) 119002, https://doi.org/10.1016/j.memsci.2020.119002.
[19] H. Li, S. Xu, B. Wang, Z. Tian, Z. Xu, F. Qian, A new insight into the effects of DMF solvent activation on the polyamide layers of nanofiltration membranes by molecular simulation, J. Membr. Sci. 718 (2025) 123667, https://doi.org/10.1016/j.memsci.2024.123667.
[20] M.G. Shin, S.J. Kwon, H. Park, Y.-I. Park, J.-H. Lee, High-performance and acid-resistant nanofiltration membranes prepared by solvent activation on polyamide reverse osmosis membranes, J. Membr. Sci. 595 (2020) 117590, https://doi.org/10.1016/j.memsci.2019.117590.
[21] Y. Li, J. Zhu, S. Li, Z. Guo, B. Van der Bruggen, Flexible aliphatic–aromatic polyamide thin film composite membrane for highly efficient organic solvent nanofiltration, ACS Appl. Mater. Interfaces 12 (28) (2020) 31962–31974, https://doi.org/10.1021/acsami.0c07341.
[22] Q. Shen, Y. Lin, P. Zhang, J. Segawa, Y. Jia, T. Istirokhatun, X. Cao, K. Guan, H. Matsuyama, Development of ultrathin polyamide nanofilm with enhanced inner-pore interconnectivity via graphene quantum dots-assembly intercalation for high-performance organic solvent nanofiltration, J. Membr. Sci. 635 (2021) 119498, https://doi.org/10.1016/j.memsci.2021.119498.
[23] Y. Shen, Y. Li, S. Yuan, J. Shen, D. Wang, N. Zhang, J. Niu, Z. Wang, Z. Wang, Polyfunctional arylamine based nanofiltration membranes with enhanced aggressive organic solvents resistance, Nano Lett. 24 (33) (2024) 10169–10176, https://doi.org/10.1021/acs.nanolett.4c02403.
[24] Y. He, Y. Zhang, F. Liang, Y. Zhu, J. Jin, Chlorine resistant polyamide desalination membrane prepared via organic-organic interfacial polymerization, J. Membr. Sci. 672 (2023) 121444, https://doi.org/10.1016/j.memsci.2023.121444.
[25] Z. Wang, K. Nakagawa, K. Guan, M. Hu, Z. Mai, W. Fu, Q. Shen, Y. Okamoto, A. Matsuoka, E. Kamio, T. Yoshioka, H. Matsuyama, Self-aggregation control of porphyrin for enhanced selective covalent organic network membranes, Small(n/a) 2407986. https://doi.org/https://doi.org/10.1002/smll.202407986.
[26] M. Sono, M.P. Roach, E.D. Coulter, J.H. Dawson, Heme-containing oxygenases, Chem. Rev. 96 (7) (1996) 2841–2888, https://doi.org/10.1021/cr9500500.
[27] M.L. Pegis, D.J. Martin, C.F. Wise, A.C. Brezny, S.I. Johnson, L.E. Johnson, N. Kumar, S. Raugei, J.M. Mayer, Mechanism of catalytic O2 reduction by iron tetraphenylporphyrin, J. Am. Chem. Soc. 141 (20) (2019) 8315–8326, https://doi.org/10.1021/jacs.9b02640.
[28] A.K. Surendran, A.Y. Pereverzev, J. Roithová, Intricacies of mass transport during electrocatalysis: a journey through iron porphyrin-catalyzed oxygen reduction, J. Am. Chem. Soc. 146 (22) (2024) 15619–15626, https://doi.org/10.1021/jacs.4c04989.
[29] K. Guan, K. Ushio, K. Nakagawa, T. Shintani, T. Yoshioka, A. Matsuoka, E. Kamio, W. Jin, H. Matsuyama, Integration of thin film composite graphene oxide membranes for solvent resistant nanofiltration, J. Membr. Sci. 660 (2022) 120861, https://doi.org/10.1016/j.memsci.2022.120861.
[30] W. Fu, L. Deng, M. Hu, Z. Mai, G. Xu, Y. Shi, K. Guan, R.R. Gonzales, A. Matsuoka, H. Matsuyama, Polyamide composite membrane with 3D honeycomb-like structure via acetone-regulated interfacial polymerization for high-efficiency organic solvent nanofiltration, J. Membr. Sci. 679 (2023) 121711, https://doi.org/10.1016/j.memsci.2023.121711.
[31] H. Lv, X.-P. Zhang, K. Guo, J. Han, H. Guo, H. Lei, X. Li, W. Zhang, U.-P. Apfel, R. Cao, Coordination tuning of metal porphyrins for improved oxygen evolution reaction, Angew. Chem. Int. Ed. 62 (38) (2023) e202305938, https://doi.org/10.1002/anie.202305938.
[32] S. Ferguson-Miller, G.T. Babcock, Heme/copper terminal oxidases, Chem. Rev. 96 (7) (1996) 2889–2908, https://doi.org/10.1021/cr950051s.
[33] M. Wang, S.-L. Li, Y. Chen, Q. Duan, D. Cheng, G. Gong, Y. Hu, Construction of ultrathin and microporous polyesteramide nanofilms for efficient organic solvent nanofiltration (OSN) using diacyl chloride, J. Membr. Sci. 698 (2024) 122605, https://doi.org/10.1016/j.memsci.2024.122605.
[34] A. Yao, J. Du, Q. Sun, L. Liu, Z. Song, W. He, J. Liu, Flexible covalent organic network with ordered honeycomb nanoarchitecture for molecular separations, ACS Nano (2023), https://doi.org/10.1021/acsnano.3c08028.
[35] J. Ren, W. Yan, X. Liu, F. Wang, Q. Xing, Z. Xiao, H. Liu, Y. Chen, X. Li, Porphyrin polymer-derived single-atom Fe assisted by Fe2O3 with oxygen vacancy for efficient oxygen reduction reaction, Appl. Surf. Sci. 592 (2022) 153301, https://doi.org/10.1016/j.apsusc.2022.153301.
[36] M.-M. Jia, J.-H. Feng, W. Shao, Z. Chen, J.-R. Yu, J.-J. Sun, Q.-Y. Wu, Y. Li, M. Xue, X.-M. Chen, In-situ interfacial synthesis of metal-organic framework/polyamide thin-film nanocomposite membranes with elevated nanofiltration performances, J. Membr. Sci. 694 (2024) 122418, https://doi.org/10.1016/j.memsci.2024.122418.
[37] D.L. Zhao, S. Japip, Y. Zhang, M. Weber, C. Maletzko, T.-S. Chung, Emerging thin-film nanocomposite (TFN) membranes for reverse osmosis: a review, Water Res. 173 (2020) 115557, https://doi.org/10.1016/j.watres.2020.115557.
[38] S. Karan, Z. Jiang, A.G. Livingston, Sub–10 nm polyamide nanofilms with ultrafast solvent transport for molecular separation, Science 348 (6241) (2015) 1347–1351, https://doi.org/10.1126/science.aaa5058.
[39] J.M. Dennison, X. Xie, C.J. Murphy, D.G. Cahill, Density, elastic constants, and thermal conductivity of interfacially polymerized polyamide films for reverse osmosis membranes, ACS Appl. Nano Mater. 1 (9) (2018) 5008–5018, https://doi.org/10.1021/acsanm.8b01129.
[40] Q.-C. Xia, M.-L. Liu, X.-L. Cao, Y. Wang, W. Xing, S.-P. Sun, Structure design and applications of dual-layer polymeric membranes, J. Membr. Sci. 562 (2018) 85–111, https://doi.org/10.1016/j.memsci.2018.05.033.
[41] J. Xu, H. Zhang, X. Ren, S. Yao, W. Fan, A. Nafady, A.M. Al-Enizi, S. Ma, A continuous porous porphyrinic polymer thin-film composite membrane for anti-biofouling and molecular sieving, J. Mater. Chem. A 12 (38) (2024) 26170–26177, https://doi.org/10.1039/D4TA04510F.
[42] P. Gorgojo, M.F. Jimenez-Solomon, A.G. Livingston, Polyamide thin film composite membranes on cross-linked polyimide supports: improvement of RO performance via activating solvent, Desalination 344 (2014) 181–188, https://doi.org/10.1016/j.desal.2014.02.009.
[43] P. Marchetti, A. Butté, A.G. Livingston, An improved phenomenological model for prediction of solvent permeation through ceramic NF and UF membranes, J. Membr. Sci. 415–416 (2012) 444–458, https://doi.org/10.1016/j.memsci.2012.05.030.
[44] S. Karan, S. Samitsu, X. Peng, K. Kurashima, I. Ichinose, Ultrafast viscous permeation of organic solvents through diamond-like carbon nanosheets, Science 335 (6067) (2012) 444–447, https://doi.org/10.1126/science.1212101.
[45] D. Shi, H. Li, X. Yu, Z. Zhang, Y.D. Yuan, W. Fan, H. Yuan, Y. Ying, H. Yang, C. Shang, J. Imbrogno, D. Zhao, Intercrystalline channels at subnanometer scale for precise molecular nanofiltration, J. Am. Chem. Soc. 145 (29) (2023) 15848–15858, https://doi.org/10.1021/jacs.3c02711.
[46] S. Zheng, Q. Tu, M. Wang, J.J. Urban, B. Mi, Correlating interlayer spacing and separation capability of graphene oxide membranes in organic solvents, ACS Nano 14 (5) (2020) 6013–6023, https://doi.org/10.1021/acsnano.0c01550.
[47] L. Nie, K. Goh, Y. Wang, J. Lee, Y. Huang, H.E. Karahan, K. Zhou, M.D. Guiver, T.-H. Bae, Realizing small-flake graphene oxide membranes for ultrafast size-dependent organic solvent nanofiltration, Sci. Adv. 6 (17) (2020) eaaz9184, https://doi.org/10.1126/sciadv.aaz9184.
[48] C.-G. Jin, W.-H. Zhang, N. Tian, B. Wu, M.-J. Yin, Q.-F. An, Fabrication of coffee-ring nanostructured membranes for organic solvent nanofiltration, Angew. Chem. Int. Ed. 63 (31) (2024) e202405891, https://doi.org/10.1002/anie.202405891.
[49] D.K. Lavallee, Kinetics and mechanisms of metalloporphyrin reactions, Coord. Chem. Rev. 61 (1985) 55–96, https://doi.org/10.1016/0010-8545(85)80002-3.
[50] E.B. Fleischer, E.I. Choi, P. Hambright, A. Stone, Porphyrin studies: kinetics of metalloporphyrin formation, Inorg. Chem. 3 (9) (1964) 1284–1287, https://doi.org/10.1021/ic50019a019.
[51] O. Horváth, R. Huszánk, Z. Valicsek, G. Lendvay, Photophysics and photochemistry of kinetically labile, water-soluble porphyrin complexes, Coord. Chem. Rev. 250 (13) (2006) 1792–1803, https://doi.org/10.1016/j.ccr.2006.02.014.
[52] E. Ploetz, H. Engelke, U. Lächelt, S. Wuttke, The chemistry of reticular framework nanoparticles: MOF, ZIF, and COF materials, Adv. Funct. Mater. (2020) 1909062, https://doi.org/10.1002/adfm.201909062.
[53] N. Zarrabi, P.K. Poddutoori, Aluminum(III) porphyrin: a unique building block for artificial photosynthetic systems, Coord. Chem. Rev. 429 (2021) 213561, https://doi.org/10.1016/j.ccr.2020.213561.